

Magnetic Field Amplification during Stellar Collisions between Low-Mass Stars

Taeho Ryu^{1,2,3*}, Alison Sills⁴, Ruediger Pakmor¹,
Selma de Mink¹, Robert Mathieu⁵

^{1*}Max-Planck Institute for Astrophysics, Karl-Schwarzschild-Str. 1,
Garching, 85748, Germany.

^{2*}JILA, University of Colorado and National Institute of Standards and
Technology, 440 UCB, Boulder, 80308, CO, USA.

^{3*}Department of Astrophysical and Planetary Sciences, 391 UCB,
Boulder, 80309, CO, USA.

⁴Department of Physics & Astronomy, McMaster University, 1280 Main
Street West, Hamilton, L8S 4M1, Canada.

⁵Department of Astronomy, University of Wisconsin-Madison, 475
North Charter Street, Madison, 53706, WI, USA.

*Corresponding author(s). E-mail(s): tryu@mpa-garching.mpg.de;
Contributing authors: asills@mcmaster.ca;
rpakmor@mpa-garching.mpg.de; sedemink@mpa-garching.mpg.de;
mathieu@astro.wisc.edu;

Abstract

Blue straggler stars in stellar clusters are a subset of stars that are bluer and appear younger than other cluster members, seemingly straggling behind in their evolution. They offer a unique opportunity to understand the stellar dynamics and populations within their hosts. In the collisional formation scenario, a persistent challenge is the excessive angular momentum in the collision product. The consequent significant mass loss during transition to a stable state leads to a star with too low a mass to be a blue straggler, unless it spins down efficiently. While many proposed spin-down mechanisms involve boosted angular momentum loss via magnetic braking within the collision product, the existence or strength of these magnetic fields has not been confirmed. Here, we report three-dimensional magnetohydrodynamical simulations of collisions between two low-mass main-sequence stars and investigate magnetic field amplification. Magnetic field energy is amplified by a factor of $10^8 - 10^{10}$, resulting in the magnetic field strength of

$10^7 - 10^8$ G at the core of the collision product, independent of collision parameters. The surface magnetic field strengths have increased up to $10 - 10^4$ G. In addition, a distinctly flattened, rotating gas structure appears around the collision products in off-axis collisions, which may be a hint of possible disk formation. Such significant magnetic amplification and potential disk formation suggest the possibility of efficient spin-down of collision products via magnetic braking and magnetic disk locking, which can result in their appearance as blue stragglers.

Keywords: Magnetohydrodynamics, Stellar collision, globular cluster, blue straggler

1 Main

Stars can collide physically in dense stellar environments, such as globular cluster cores. For typical stellar densities of globular clusters, up to tens of percent of stars in the center can undergo a single collision in their lifetime [1, 2]. These collisions are not sufficiently energetic, so the two stars merge into a more massive star, rather than both stars being destroyed. Because of chemical mixing, heat injection, and rotation induced by collision, the collision products can manifest as blue stragglers [3, 4]—a group of stars that appear bluer and younger than their counterparts and are located differently from most cluster members on color-magnitude diagrams [1, 5]. Stellar collisions, facilitated by multi-body interactions involving binaries [6–8], may serve as the dominant formation channel for blue stragglers in dense clusters [9]. These stars can provide unique information about the evolution history of clusters and stellar populations within them.

The properties of collision products have been studied using hydrodynamics simulations [e.g., 10–12] and their subsequent long-term evolution using stellar evolution simulations [e.g., 5, 13, 14]. These studies have shown that collision products are out of thermal equilibrium upon collision and, therefore, they are swollen in size. In addition, unless the collision is perfectly head-on, the collision product contains angular momentum comparable to or possibly larger than the theoretical upper limit of the angular momentum for a normal star of the same mass [11, 12, 15]. This naturally leads the collision product to lose a significant fraction of its mass and angular momentum during transition to a thermal equilibrium state [11, 12], unless it spins down efficiently. This excessive angular momentum of the collision product posed an ‘angular momentum’ problem for the formation of blue stragglers [12], where if the collision product loses too much mass before it spins down, the outcome would have too low mass to appear as blue stragglers.

Consequently, whether collisions are a plausible mechanism for the formation of blue stragglers comes down to a key question: can the collision product spin down efficiently? While a few spin-down mechanisms have been proposed, most of them require the existence of magnetic fields within the star, such as magnetic braking [16–18]. In addition to the direct impact of magnetic fields on the spin, it has been known that magnetic fields can also significantly affect the internal structure of the star, namely, the redistribution of angular momentum and chemical elements inside

rotating stars [19], and, therefore, even their final fate. Despite the importance of magnetic fields, the magnetic field strength and configuration inside collision products remain highly uncertain and no work on this subject using magnetohydrodynamics simulations in the context of blue stragglers has been done in the last decade.

In this article, we investigate the amplification of magnetic fields during collisions between realistic low-mass main-sequence stars, their field configuration and internal structure, using moving-mesh magnetohydrodynamics simulations.

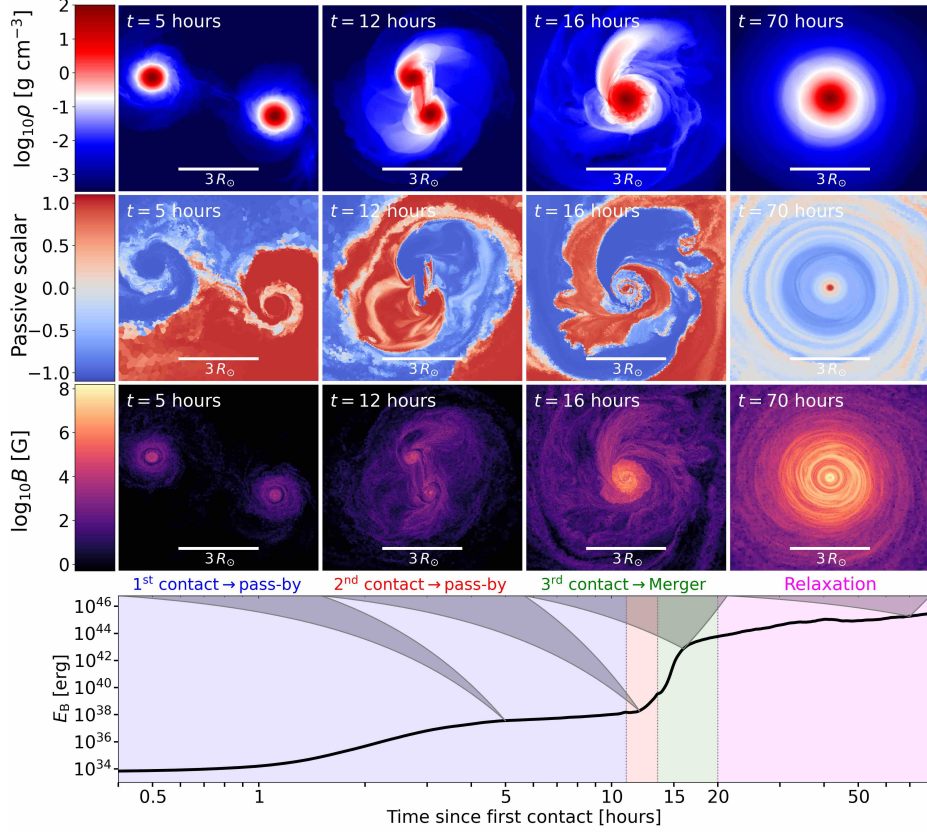


Fig. 1 Growth of the magnetic field energy E_B (line plot at the bottom) as a function of time in the collision between $0.7 M_\odot$ and $0.6 M_\odot$ stars with an impact parameter of $b = 0.5$. The panels above the line plot depict the distributions of the density ρ (top row), the passive scalar (middle row), and the magnetic field strength B (bottom row) at four different times. After the two stars make the first contact at $t = 0$ hours, they pass by ($t = 5$ hours). Magnetic fields start to grow due to instabilities and compression caused by the first encounter. However, they stop growing while the two stars are effectively isolated. Soon, they encounter ($t \simeq 11$ hours) and pass by again. The less massive star is destroyed at the third contact ($t \simeq 14$ hours) and mixed into the more massive star ($t \simeq 16$ hours), during which magnetic fields grow at the fastest rate. The amplification rate dramatically decreases while the collision product is being relaxed to recover a dynamically steady state ($t \gtrsim 20$ hours).

2 Results

We performed simulations of parabolic¹ collisions between main-sequence stars such as those found in globular clusters, using the moving-mesh magnetohydrodynamics code AREPO [21–23]. We consider mass ratios between the two colliding stars ranging from 0.5 to 0.97, with primary masses close the main-sequence turn-off mass for globular clusters at 12 Gyr [24] ($M_1 = 0.7$ and $0.8 M_\odot$). The choice of the primary masses can be justified, as more massive stars tend to accumulate near the core, where collisions are most frequent, due to mass segregation. The impact parameter $b = r_p / (R_1 + R_2)$ ranges from 0.1 to 0.5, covering from nearly head-on collisions ($b = 0.1$) to strong grazing encounters ($b = 0.5$). Here, r_p is the pericenter distance and R_1 (R_2) is the radius of the primary (secondary) star. See Table A1 for the complete list of our models with the initial collision parameters.

We assume the magnetic field of the original stars is described by a dipole field with a surface magnetic field strength of $B_s = 1\text{G}$, which is comparable to or smaller than the average magnetic field strength of the Sun [25–27], and smaller than that of M-dwarf stars [28]. The resolution is such that there are 100 – 125 cells per stellar radius of the original star, corresponding to the mass resolution of 5×10^{-7} of the stellar mass on average and the numerical Reynolds number (Equation 2 in [29]) is $\simeq 1200 - 3000$, assuming that the turbulent injection scale $\simeq 0.5(R_1 + R_2)$. See §A for more details of our methods.

2.1 Magnetic field amplification and saturation

The magnetic field energy E_B has increased by a factor of $10^8 - 10^{10}$, reaching $E_B \simeq 10^{44} - 10^{45}$ erg, by the time the collision product has recovered a dynamically steady state, independent of the masses of the colliding stars, impact parameters, and initial field strength and orientation. As a representative case, Fig. 1 illustrates the evolution of the magnetic field energy, along with the density, passive scalar, and magnetic field strength distributions, for the collision between $0.7 M_\odot$ and $0.6 M_\odot$ stars with $b = 0.5$. The passive scalar is an artificial scalar quantity initially assigned to each cell, which then evolves through advection but does not influence the evolution of hydrodynamics quantities. In this case, the two stars touch three times (at $t \lesssim 13$ hours), after which the less massive star is destroyed and mixed into the more massive star ($t \simeq 13 - 20$ hours). The merger product enters a relaxation phase ($t \gtrsim 20$ hours), the magnetic energy has reached $\simeq 10^{45}$ erg and the growth rate has dropped substantially. See the left panel of Fig. 2 for collisions between the same stars with different impact parameters and Fig. C3 for the rest of the models.

As illustrated by the representative case in Fig. 1, the collision process can be generally split into three stages, 1) contact, 2) merger, and 3) dynamical relaxation. In these collisions, there can be multiple moments of contact between the two stars before they finally merge. At each of these close approaches, turbulent and shearing flows

¹This assumption for the orbit is reasonable, considering that the typical eccentricity for collisions in globular clusters with velocity dispersion $\sigma \simeq 10 - 15 \text{ km s}^{-1}$ [20] can be estimated as $|1 - e| \simeq 3 \times 10^{-4} (\sigma / 10 \text{ km s}^{-1})^2 (M / 2 M_\odot)^{-1} (r_p / 1 R_\odot)$, where M is the total mass of two colliding objects. For this estimate, we assume that the relative specific kinetic energy $\simeq 0.5\sigma^2$ and the specific angular momentum is $\simeq \sqrt{2GM}r_p$.

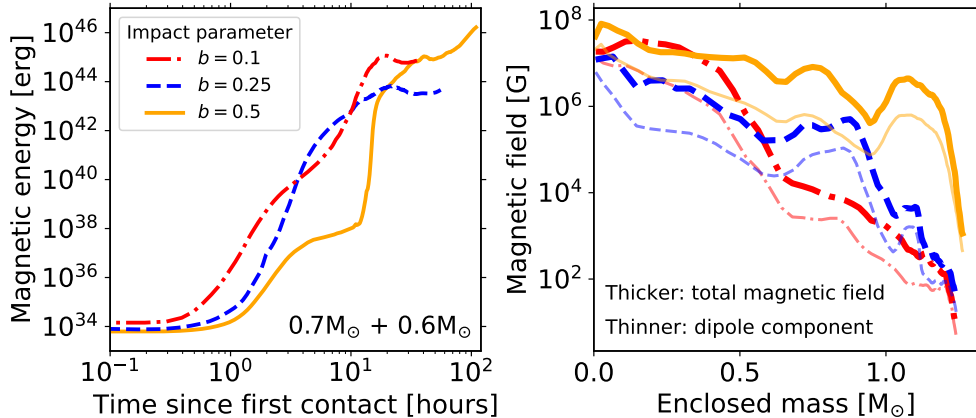


Fig. 2 (Left) Evolution of the total magnetic field energy E_B for collisions between $0.7 M_\odot$ and $0.6 M_\odot$ stars, as representative cases, with three different impact parameters b , as a function of time since the first contact. The growth rate varies, depending on the number of contacts before the final merger. However, in all cases, E_B grows by more than eight orders of magnitude over a few tens of hours via small-scale dynamos, and then saturates at $10^{44} - 10^{45}$ erg or rises substantially more slowly. (Right) Radial magnetic field strength of the products, mass-weighted averaged over the spherical equipotential surfaces, as a function of the enclosed mass. The thinner lines indicate the dipole component defined as $\sqrt{(B^r)^2 + (B^z)^2}$.

amplify magnetic fields. This naturally leads to multiple episodes of sudden increases in E_B until it saturates, as illustrated in Figs. 1 and 2. This is clearly different from the magnetic field amplification of inspiral binary mergers [30, 31] where E_B increases relatively smoothly. The number of close encounters depends primarily on the impact parameter. For nearly head-on collisions (e.g., $b = 0.1$), the two stars merge almost immediately after the first contact, during which E_B increases exponentially. However, for off-axis collisions (e.g., $b \gtrsim 0.25$), they encounter more than once before the final merger, during which the growth of E_B is not well-described by a single exponential or power-law curve.

By the time the collision product enters the relaxation phase, the total magnetic field energy saturates at a similar level ($10^{44} - 10^{45}$ erg) in all our models, with a tendency of being distributed more towards the mid-plane. The small-scale dynamo theory predicts that the magnetic energy saturates when it becomes comparable to turbulent kinetic energy [28, 32–35], which is consistent with our simulations (see Fig. C4). We also confirmed that the saturation level is robust against the resolution and initial B strength, which further supports that the small-scale dynamo would be responsible for the magnetic field amplification.

The magnetic field energy has saturated or grows noticeably more slowly in the dynamically relaxed products. By that time, most of the magnetic fields also are expected to have been relaxed. Almost all E_B is stored within 50% (90%) of the total mass of the collision products for $b \leq 0.25$ (0.5), where the local Alfvénic timescales are found to be shorter than the evolution time (see Fig. C5). Despite the dramatic amplification, the magnetic field energy comprises only a small fraction ($\lesssim 10^{-4}$) of

the total energy (see Fig. C4). As expected, the magnetic pressure does not exceed the gas + radiation pressure across the product – the ratio of the gas+radiation pressure to the magnetic pressure, also known as the plasma β , $\simeq 10$ at the core and > 10 at the envelope.

The dominant component of E_B (as well as the kinetic energy) within the collision products is the azimuthal component (see Fig. C4), with the saturated magnetic field strength B near the center $\simeq 10^7 - 10^8$ G, as shown in the right panel of Fig. 2. In general, the gradient of B , relative to the enclosed mass, is shallower for higher impact parameters (b) – the surface B is a few G for $b = 0.1$, while it is $\simeq 10^3$ G for $b = 0.5$. The mass-weighted average of magnetic flux is $\simeq 10^{26} - 10^{28}$ G cm² and surface magnetic flux of $10^{23} - 10^{26}$ G cm². If the magnetic flux is conserved, the surface magnetic field of the thermally relaxed collision product would be $10 - 10^4$ G. The dipole field ($\sqrt{(B^r)^2 + (B^z)^2}$, where B^r is the radial component and B^z is the vertical component), more relevant for the magnetic braking and, thus, the spin down of the merger product, is consistently smaller than the total field by a factor of a few.

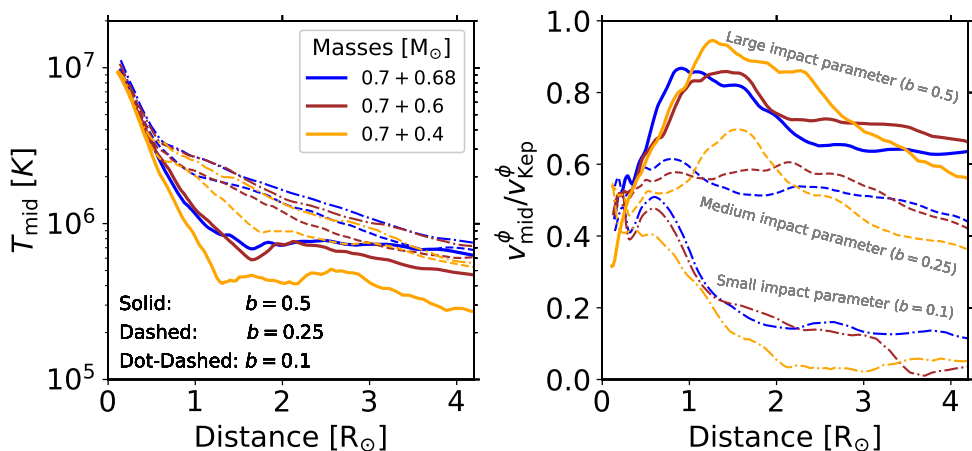


Fig. 3 Mass-weighted average of the temperature T_{mid} in the mid-plane (left) and the ratio of the rotational velocity in the mid-plane to the Keplerian velocity $v_{\text{mid}}^{\phi}/v_{\text{Kep}}^{\phi}$, as a function of distance from the center of mass of the collision products in collisions involving $M_1 = 0.7 M_{\odot}$, with different impact parameters b . The temperature profile shows a noticeable slope change at $0.7 - 0.8 R_{\odot}$ for $b \leq 0.25$ (except for one case with $M_2 = 0.4 M_{\odot}$ and $b = 0.25$) and $1 - 2 R_{\odot}$ for $b = 0.5$ (solid lines). The velocity ratio profiles show the similar features.

2.2 Disk formation

In addition to magnetic braking by winds, magnetic disk locking has been proposed [e.g., 36, 37] as another potential spin-down mechanism for blue stragglers [e.g., 12]. However, whether a disk forms around collision products is highly uncertain [e.g., 12, 38]. Our simulations show that as the impact parameter increases, the surrounding

envelopes become more oblate (e.g., see also Fig. E10), which is not surprising given the larger angular momentum. One notable feature of the products in collisions with $b = 0.5$ is the appearance of a distinctly flattened structure along the mid-plane, comprising a few % of the collision product’s mass. In addition, we find that temperature and velocity profiles along the mid-plane show a sharp change in slope where the flattened structure manifests, as demonstrated in Fig. 3. The slope break becomes clearer for larger b . However, the flattened region does not resemble a Keplerian thin disk. Rather, at this stage, it is geometrically thick and radiation-pressure supported – the aspect ratios are $0.2 - 0.5$ and the ratios of the rotational velocity to the Keplerian speed are $0.1 - 0.8$. This region of gas would cool down on a time scale comparable to the photon diffusion time, which is approximately $10^3 - 10^4$ years at $\rho \simeq 10^{-2} \text{ g cm}^{-3}$. Although it is difficult to determine whether the envelopes would eventually settle into a disk or merge into the star based on the limited timescale of our adiabatic simulations, the appearance of the distinctly flattened structure may be indicative of disk formation.

3 Discussion and Summary

Significant magnetic field amplification and the possible disk formation found in our simulations are promising signs for the potentially significant role of magnetic fields in the long-term evolution of collision products, i.e., their spin and internal structure. If collision products can maintain strong surface magnetic fields for a sufficiently long time, i.e., a significant fraction of blue stragglers’ lifetime of a few Gyr [5], magnetic braking could spin down the products efficiently. We estimate that the spin-down time scale via magnetic braking $\simeq 0.1 \text{ Gyr} (B_s/100 \text{ G})^{-1} (\dot{M}/10^{-10} \text{ M}_\odot \text{ yr}^{-1})^{-0.5}$ assuming the surface is magnetized and rigidly rotating, ejecting mass at a rate \dot{M} [39, 40]. In addition to magnetic braking, if a disk forms ultimately and its lifetime is long (more than a few Myrs [12]), magnetic disk locking would also contribute to the spin-down of collision products. Further support for efficient spin-down via magnetic locking mechanisms is the observed tendency of blue stragglers to exhibit slower rotation rates in denser stellar environments, where stellar collisions are expected to occur [41].

Although our simulations make a strong case for magnetic field amplification, several questions still remain to be answered. The first is whether the magnetic field amplification found in our simulations can occur in nature, given the non-zero viscosity and resistivity in stars, which we do not take into account. As an order of magnitude estimate, taking the expression for the magnetic Prandtl number P_m for a pure, collisional hydrogen plasma (Equation 2.23 in [42]), we find that $P_m \simeq 10^{-1} - 10^{-2}$ for typical temperatures and densities during collisions in our simulations. This is on the same order as the expected P_m of low-mass main-sequence stars and falls within the range of P_m values for the Sun. Previous numerical simulations showed that dynamos can effectively amplify magnetic fields in a plasma with large P_m [e.g., 43]. However, relatively recent numerical simulations indicated that field amplification in a plasma with $P_m \gtrsim 10^{-3}$ via small-scale dynamos is also possible if the magnetic Reynolds number is sufficiently high [e.g., 44, 45].

Second, even if magnetic fields are amplified during collisions, the timescale over which these amplified magnetic fields dissipate is highly uncertain. This would depend

on many factors, such as how efficiently dynamos operate in the long term and whether magnetic fields within the collision products can achieve a stable configuration. These questions directly pertain to the effect of spin-down via the magnetic braking and disk locking mechanisms. While our results cannot provide a definitive answer to the questions, the presence of non-zero polar and radial magnetic field components suggest that a stable configuration can be achieved via the $\alpha\omega$ dynamo effect. Nonetheless, to a zeroth-order approximation, magnetic fields will dissipate on a timescale comparable to the Ohmic dissipation timescale without a continuous source of dynamo action. Using the Spitzer’s resistivity [46] $\eta \simeq 10^4 \ln \Lambda (T/10^6 K)^{-3/2} \text{cm}^2 \text{s}^{-1}$, where $\ln \Lambda \simeq 15$ is the Coulomb logarithm, the Ohmic timescale for stars with mass comparable to those of the collision products in our simulations would be roughly $\simeq 0.1(T/10^6 K)^{3/2} (l/0.1 R_\odot)^2$ Gyr. Here, l is the radial distance scale between mid-plane magnetic fields in the ϕ direction with opposite directions in the dynamically relaxed collision products. This diffusion time, comparable to the thermal relaxation time of collision products, may indicate the possibility of the long-term role of magnetic braking or even disk locking (if a disk forms) in spinning down the collision products if they achieve a stable configuration.

Even if all the conditions for dynamo action and long magnetic field dissipation timescales are met, it is crucial to examine the long-term evolution of collision products with proper treatments of mixing and magnetic fields to confirm whether they indeed appear as blue stragglers. Additionally, it is important to understand any unique observational signatures of this formation channel, distinguishable from other formation channels. While we leave these important topics for future studies, we believe our simulations results can serve as useful initial conditions for stellar evolution simulations for collision products with magnetic fields.

Acknowledgements. TR is thankful to Matteo Cantiello, Benjamin Brown, Chen Wang, James Lombardi, and Valentin Skoutnev for useful discussions and suggestions. AS is supported by the Natural Sciences and Engineering Research Council of Canada. RDM acknowledges the support of the Wisconsin Alumni Research Fund. This research project was conducted using computational resources (and/or scientific computing services) at the Max-Planck Computing & Data Facility. The authors gratefully acknowledge the scientific support and HPC resources provided by the Erlangen National High Performance Computing Center (NHR@FAU) of the Friedrich-Alexander-Universität Erlangen-Nürnberg (FAU) under the NHR projects b166ea10 and b222dd10. NHR funding is provided by federal and Bavarian state authorities. NHR@FAU hardware is partially funded by the German Research Foundation (DFG) – 440719683. In addition, some of the simulations were performed on the national supercomputer Hawk at the High Performance Computing Center Stuttgart (HLRS) under the grant number 44232.

Appendix A Methods

We take the initial state of main-sequence stars, computed using the stellar evolution code MESA (version r24.03.1) [47–51]. We adopt the prescriptions for convection, overshoot, semiconvection, and thermohaline mixing from [52]. We use the Ledoux

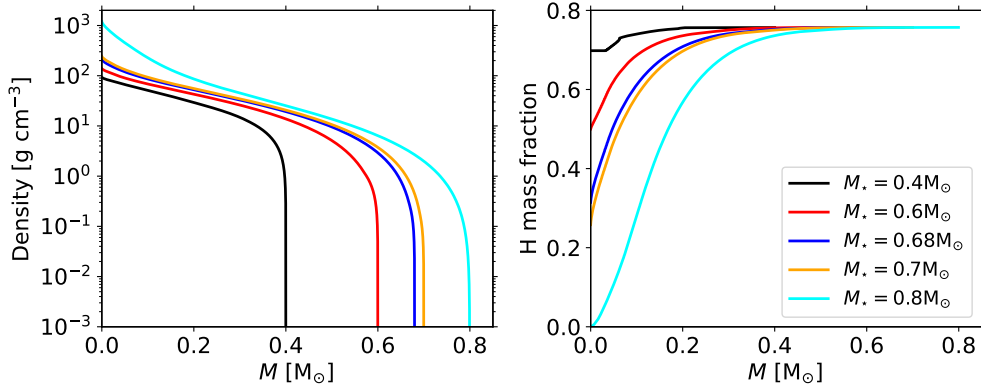


Fig. A1 Density and hydrogen mass fraction profiles of initial models for main-sequence stars with a metallicity of $Z = 0.001$ and at an age of 12 Gyr, as a function of enclosed mass.

Table A1 Model list and initial parameters, and properties of dynamically relaxed collision products. The initial collision parameters are provided up to the fifth column: mass of the original primary star $M_1[M_\odot]$, mass of the original secondary star $M_2[M_\odot]$, mass ratio M_2/M_1 , and pericenter distance $b = r_p/[R_1 + R_2]$. The rest columns indicate the properties of the collision product: mass M , angular momentum L , potential energy E_{pot} , thermal (gas + radiation) energy E_{therm} , radial kinetic energy E_{K}^r , azimuthal kinetic energy E_{K}^θ , vertical kinetic energy E_{K}^z , radial magnetic energy E_{B}^r , azimuthal magnetic energy E_{B}^θ , vertical magnetic energy E_{B}^z , and surface magnetic flux Φ_{B} . Units: M in M_\odot , L in $\text{g cm}^2\text{s}^{-1}$, all energies in 10^{43}erg , and Φ_{B} in G R_\odot^2 .

-	M_1	M_2	q	b	M	L	E_{pot}	E_{therm}	E_{K}^r	E_{K}^θ	E_{K}^z	E_{B}^r	E_{B}^θ	E_{B}^z	Φ_{B}
1	0.7	0.68	0.97	0.10	1.34	1.2	-8.3×10^5	3.6×10^5	30	5.7×10^4	15	1.8	81	1.1	34
2	0.7	0.68	0.97	0.25	1.34	2.0	-7.7×10^5	3.0×10^5	68	8.5×10^4	30	0.9	21	0.17	200
3	0.7	0.68	0.97	0.50	1.37	2.9	-7.7×10^5	2.8×10^5	130	11×10^4	15	13	480	3.2	8000
4	0.7	0.60	0.86	0.10	1.26	1.1	-7.5×10^5	3.3×10^5	41	5.1×10^4	18	2.8	76	0.91	46
5	0.7	0.60	0.86	0.25	1.27	1.7	-7.0×10^5	2.8×10^5	140	6.9×10^4	21	0.2	4.3	0.06	180
6	0.7	0.60	0.86	0.50	1.30	2.5	-6.8×10^5	2.6×10^5	240	8.5×10^4	28	84	1500	28	10100
7	0.7	0.40	0.57	0.10	1.08	0.7	-6.1×10^5	2.7×10^5	190	3.7×10^4	64	1.8	22	0.38	9
8	0.7	0.40	0.57	0.25	1.09	1.2	-5.8×10^5	2.4×10^5	280	5.1×10^4	29	2.1	54	0.36	160
9	0.7	0.40	0.57	0.50	1.10	1.6	-5.6×10^5	2.2×10^5	890	5.9×10^4	40	1.9	27	0.57	16000
10	0.8	0.70	0.87	0.10	1.45	1.6	-9.6×10^5	4.0×10^5	190	7.7×10^4	53	0.7	30	0.33	60
11	0.8	0.70	0.87	0.25	1.47	2.6	-9.1×10^5	3.5×10^5	300	11×10^4	150	1.5	33	0.59	160
12	0.8	0.60	0.75	0.10	1.36	1.4	-8.5×10^5	3.6×10^5	91	7.0×10^4	31	12	180	9.0	98
13	0.8	0.60	0.75	0.25	1.38	2.2	-8.2×10^5	3.2×10^5	230	9.1×10^4	124	4.7	16	4.8	150
14	0.8	0.40	0.50	0.10	1.18	1.0	-7.3×10^5	3.1×10^5	54	5.1×10^4	41	1.0	40	2.1	12
15	0.8	0.40	0.50	0.25	1.20	1.6	-7.0×10^5	2.9×10^5	1900	5.6×10^4	300	4.3	23	3.6	140

criterion [53] to identify the boundary of the convective regions. We consider a range of stellar masses from $0.4 - 0.8 M_\odot$ at the stellar age of 12 Gyr and a metallicity $Z = 0.001$, relevant for old stars in globular clusters [e.g., 24]. We depict the density and H mass fraction profiles of our stellar models in Fig. A.

We perform a suite of 3D magnetohydrodynamic (MHD) simulations of stellar collisions using the massively parallel gravity and MHD moving-mesh code AREPO [21–23]. By adopting the novel approach of a moving mesh, AREPO inherits advantages of

Eulerian finite-volume methods and Lagrangian particle methods, resulting in accurate shock capturing without introducing an artificial viscosity, small advection errors, and an efficient tracking of supersonic flows. The code has been used to study a variety of astrophysics problems, ranging from cosmology [e.g., 54, 55], tidal disruption events [e.g., 15, 56–58], to common envelop [e.g. 59], binary mergers [e.g., 30, 60, 61], and stellar collisions [62]. We adopt the OPAL equation of state [63] and follow the advection of five isotopes (H, ^4He , ^{12}C , ^{14}N , ^{16}O). We employ the Powell scheme [64] for B -field divergence control. For implementation details in AREPO, and code tests, we refer to [65, 66].

Our MHD simulations of stellar collisions involve two steps. In the first step, we create a 3D MS star for each MESA model using the mesh construction method by [67]. We evolve the stars in isolation until they are fully relaxed, which takes less than 5 - 10 t_{dyn} . Here, the stellar dynamical time is defined as $t_{\text{dyn}} = \sqrt{R_\star^3/GM_\star}$ where M_\star (R_\star) is the stellar mass (radius). For the stars considered, $t_{\text{dyn}} = O(10^2 - 10^3)$ s. During this relaxation phase, we ignore the magnetic field inside the stars because the seed magnetic field (1G at the stellar surface) is so small that the magnetic pressure is completely negligible compared to the thermal (gas + radiation) pressure.

In the second step, we conduct collision experiments, by placing two fully relaxed MS stars on a parabolic orbit, initially separated by $8(R_1 + R_2)$. Here, R_1 and R_2 are the radii of the colliding stars. The orbital axis is always aligned with the z axis of the domain. We assume the seed magnetic field inside the star can be described by the dipole field along the z direction,

$$\mathbf{B}(r) = \frac{B_s}{2} \frac{3\hat{\mathbf{r}}(\hat{\mathbf{b}} \cdot \hat{\mathbf{r}}) - \hat{\mathbf{b}}}{(r/R_\star)^3}, \quad (\text{A1})$$

where B_s is the stellar surface field strength at the pole, $\hat{\mathbf{r}}$ the unit position vector inside the star, and $\hat{\mathbf{b}}$ the unit dipole vector. We assume $B_s = 1\text{G}$, which is comparable to or smaller than the average magnetic field strength of the Sun [25–27], and smaller than that of M-dwarf stars [28]. As Equation A1 indicates, the magnetic field increases inward inside the star. To be conservative, we limit the seed magnetic field to be less than $100B_s$.

Using this numerical setup, we investigate the dependence of collision outcomes on several key collision parameters: the stellar masses M_1 and M_2 , and pericenter distance $b = r_p/(R_1 + R_2)$. We consider $b = 0.1, 0.25$, and 0.5 . We provide the complete list of models in Table A1.

We follow the evolution until a collision product forms and becomes fully relaxed dynamically whose internal structure (e.g., density, angular frequency, and magnetic field strength) does not change over time. The timescale of the collision process, from the initial contact to dynamical relaxation, is shorter for a smaller impact parameter. It takes around 20 - 50 hours since collision for $b \leq 0.25$, > 50 hours for $b = 0.5$.

In all simulations, the fractional errors in total energy remain small (\lesssim a few %) until the end of the simulations.

To ensure the robustness of our simulations, we performed resolution tests as well as additional simulations with different initial magnetic field strengths, which will be explained in detail in Appendix B.

Appendix B Tests on resolution, initial magnetic field strength and configuration

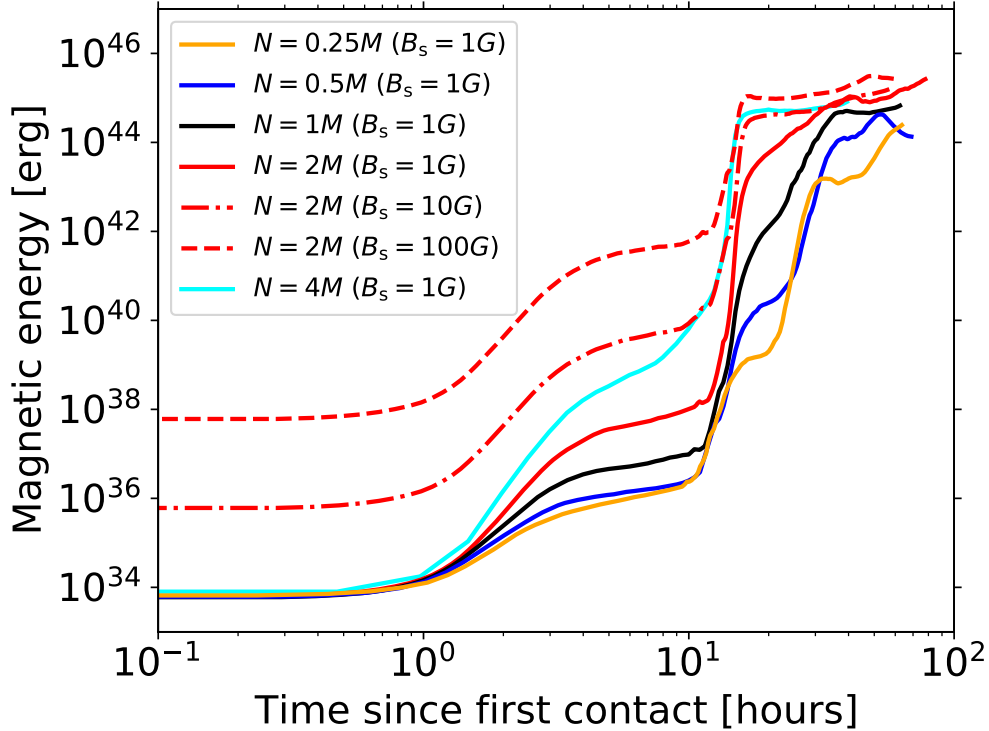


Fig. B2 Evolution of the total magnetic field energy E_B as a function of time with varying number of cells per star N (0.25M to 4M, different colors) and the initial magnetic field strength at the stellar surface B_s (1G, 10G, and 100G, different line styles). The magnetic energy saturates at similar levels, independent of N and B_s .

To ensure the robustness and convergence of our results for magnetic field amplification, we conducted additional simulations with different seed magnetic field strengths ($B_s = 1G$, 10G, and 100G), varying resolution from $N = 0.25M$ to $N = 4M$ (where N is the number of cells per star), and different initial dipole orientations. The resolution range corresponds to an average cell size from $0.025R_*$ to $0.01R_*$. Note that because two stars merge into one during collision with negligible mass loss, the collision products have almost twice as many cells. As shown in Fig. B2, we found that while the resolution affects magnetic field amplification rates, the total saturated magnetic field energy inside merger products consistently reached a similar level. Moreover, we tested the dependence on the orientation of the initial dipole configurations for slight different cases ($0.6M_\odot + 0.6M_\odot$), and found that it barely affected the saturated magnetic field energy.

Appendix C Magnetic field energy and energy hierarchy

In Fig. C3, we compare the total magnetic field energy $E_B = \int B^2/(8\pi)dV$ inside the collision products for all our models except our fiducial models for $M_1 = 0.7 M_\odot$ and $M_2 = 0.6 M_\odot$. In Fig. C5, we depict the accumulative magnetic field energy $E_B(< R) = \int_0^R \int_0^\pi \int_0^{2\pi} B(r, \theta, \phi)^2/(8\pi) dr d\theta d\phi$. Finally, the ratios of the thermal energy, kinetic energy, and magnetic energy to the absolute potential energy are depicted in Fig. C4.

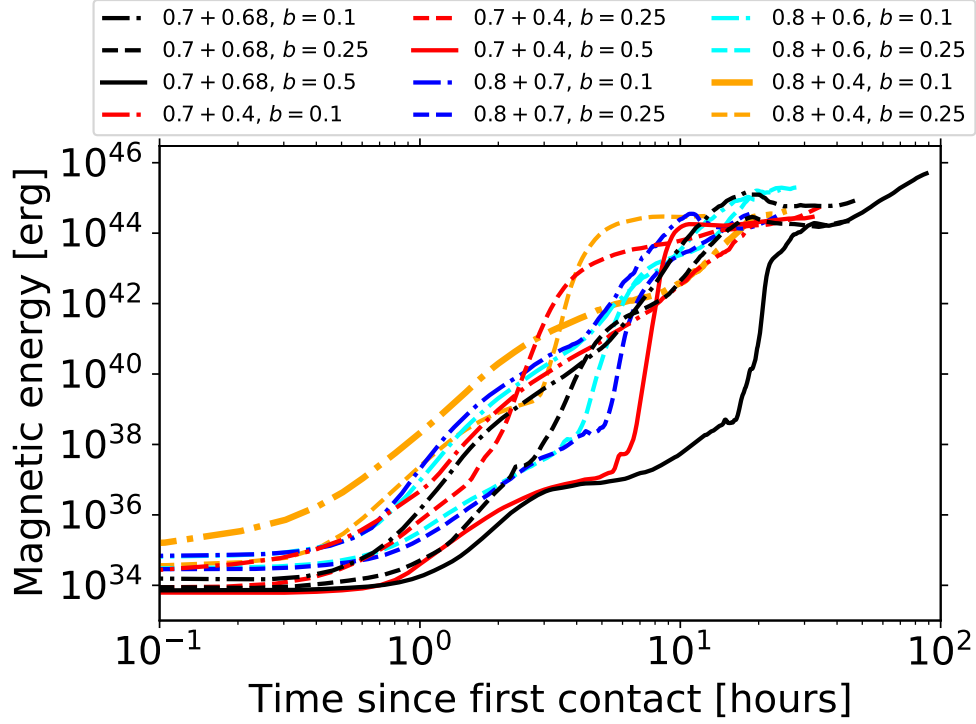


Fig. C3 Evolution of the total magnetic field energy E_B for all the models other than the fiducial models, as a function of time since the first contact. E_B has reached at $10^{44} - 10^{45}$ erg, independent of the initial collision parameters.

Appendix D Angular momentum and mixing within collision products

Dynamically relaxed collision products are differentially rotating, bloated, and magnetized. The total angular momentum of the collision products in all models falls within

a range of $\simeq (1 - 3) \times 10^{51} \text{ g cm}^2 \text{ s}^{-1}$ (see Table A1). This is comparable to the maximum possible angular momentum that an ordinary main-sequence star of the same mass can have, which is consistent with previous work [11, 12]. Generally, the ratios of the spin frequency to the local critical value for collisions with $M_1 = 0.7 M_\odot$ are $0.4 - 0.6$ across the products except for $b = 0.1$ in which the ratio near the surface decreases below 0.4 (see the top panels of Fig D6). For collisions with $M_1 = 0.8 M_\odot$, the frequency ratios tend to be somewhat smaller, $0.2 - 0.6$, because the primary is more centrally concentrated (closer to terminal-age main-sequence), making it less subject to perturbations by the encounters. The mid-plane surface velocities are within the range of $50 - 200 \text{ km/s}$ (see the bottom panels of Fig. D6).

Chemical elements are mixed during collisions. The hydrogen mass fraction X_{H} at the central part of the collision product is always higher than that of the original primary star (see Fig. D7). The increase in core X_{H} is more significant in collisions between two stars with less comparable masses on an evolutionary stage closer to zero-age main-sequence (lower central density), with smaller impact parameters. The core X_{H} of the final product in collisions with $M_1 = 0.7 M_\odot$ star has reached to $\simeq 0.6$ when $b \lesssim 0.25$, corresponding to an increase by a factor of two than that of the primary parent star. The increase in the core X_{H} in the collisions involving the same primary star with $b = 0.5$ is negligible. On the other hand, in collisions with $M_1 = 0.8 M_\odot$, the core X_{H} of the most collision products is very similar to that of the $0.8 M_\odot$ star, except the collision between $0.8 M_\odot$ and $0.7 M_\odot$ stars, where the core X_{H} increases by 0.2 .

X_{H} is generally lower in the envelope of the collision product than that of the two parent stars at the same fractional mass coordinate (see Fig. D7). As a result, the gradient of X_{H} or dX_{H}/dM is generally lower than that of both original stars. This indicates that while the two stars are mixed as they merge, there is additional injection of gas which originally belonged to the envelopes into the central part of the collision product.

Chemical composition profiles of the collision products were often predicted by sorting the entropy of the parent stars [68]. Mixing in most of our simulations for the collisions of the $0.8 M_\odot$ star is in good agreement with what is predicted by the entropy sorting method. However, our simulations suggest that mixing in collisions with $M_1 = 0.7 M_\odot$ is more efficient (see Fig. D7). In particular, for small- b collisions, the core X_{H} in our simulations is higher by $30 - 50\%$ than what is predicted with the entropy sorting.

The level of mixing depends on the primary mass, the central density ratio, and the impact parameter. Here, we define the central density ratio in the same way as the mass ratio, namely, $\rho_{c,2}/\rho_{c,1} \leq 1^2$. Mixing becomes more efficient in collisions between two stars with more comparable masses on a evolutionary stage closer to zero-age main-sequence (lower central density), with smaller impact parameters. We illustrate this trend in Fig. D8 showing the fraction of mass within the central part of collision products that initially belonged to the original primary star. When two stars with similar masses collide (blue markers), mixing is maximized and two stars are almost equally mixed, independent of b . However, when the same primary collides

²Note that for main-sequence stars at the same age, the central density ratio follows the similar trend as the mass ratio: For the same primary mass, the central density ratio decreases with the mass ratio.

with a lower-mass star (red and magenta markers), mixing begins to depend on b : less efficient mixing occurs with larger b . It is because, as the mass ratio becomes smaller (equivalently smaller central density ratio for the same primary at the same age), the primary's core remains more intact while the secondary is destroyed and mixed into the envelope of the primary during encounters. For given age and mass ratio, as the primary becomes more massive (hollow markers compared to the solid markers), mixing becomes less efficient as the primary becomes more centrally concentrated and becomes harder to perturb.

Appendix E Profiles of outer envelopes

We depict in Fig. E10 the density distribution of the products in collisions with $M_1 = 0.7M_\odot$ and $M_2 = 0.68M_\odot$ with three different impact parameters, i.e., $b = 0.1$ (left), 0.25 (middle), and 0.5 (right), along a vertical slice passing through the center of mass.

References

- [1] Hills, J.G., Day, C.A.: Stellar Collisions in Globular Clusters. *Astrophysics Letters* **17**, 87 (1976)
- [2] Dale, J.E., Davies, M.B.: Collisions and close encounters involving massive main-sequence stars. *Mon. Not. R. Astron. Soc.* **366**(4), 1424–1436 (2006) <https://doi.org/10.1111/j.1365-2966.2005.09937.x> [arXiv:astro-ph/0602042](https://arxiv.org/abs/astro-ph/0602042) [astro-ph]
- [3] Sandage, A.R.: The color-magnitude diagram for the globular cluster M 3. *Astron. J.* **58**, 61–75 (1953) <https://doi.org/10.1086/106822>
- [4] Burbidge, E.M., Sandage, A.: The Color-Magnitude Diagram for the Galactic NGC 7789. *Astrophys. J.* **128**, 174 (1958) <https://doi.org/10.1086/146535>
- [5] Sills, A., Karakas, A., Lattanzio, J.: Blue Stragglers After the Main Sequence. *Astrophys. J.* **692**(2), 1411–1420 (2009) <https://doi.org/10.1088/0004-637X/692/2/1411> [arXiv:0811.2974](https://arxiv.org/abs/0811.2974) [astro-ph]
- [6] Leonard, P.J.T.: Stellar Collisions in Globular Clusters and the Blue Straggler Problem. *Astron. J.* **98**, 217 (1989) <https://doi.org/10.1086/115138>
- [7] Leonard, P.J.T., Fahlman, G.G.: On the Origin of the Blue Stragglers in the Globular Cluster NGC 5053. *Astron. J.* **102**, 994 (1991) <https://doi.org/10.1086/115927>
- [8] Leonard, P.J.T., Linnell, A.P.: On the Possibility of a Collisional Origin for the Blue Stragglers and Contact Binaries in the Old Open Cluster M67 and NGC 188. *Astron. J.* **103**, 1928 (1992) <https://doi.org/10.1086/116202>
- [9] Chatterjee, S., Rasio, F.A., Sills, A., Glebbeek, E.: Stellar Collisions and Blue Straggler Stars in Dense Globular Clusters. *Astrophys. J.* **777**(2), 106 (2013)

- <https://doi.org/10.1088/0004-637X/777/2/106> arXiv:1302.7284 [astro-ph.SR]
- [10] Hills, J.G.: Hyper-velocity and tidal stars from binaries disrupted by a massive Galactic black hole. *Nature* **331**, 687–689 (1988) <https://doi.org/10.1038/331687a0>
- [11] Sills, A., Faber, J.A., Lombardi, J. James C., Rasio, F.A., Warren, A.R.: Evolution of Stellar Collision Products in Globular Clusters. II. Off-Axis Collisions. *Astrophys. J.* **548**(1), 323–334 (2001) <https://doi.org/10.1086/318689> arXiv:astro-ph/0008254 [astro-ph]
- [12] Sills, A., Adams, T., Davies, M.B.: Blue stragglers as stellar collision products: the angular momentum question. *Mon. Not. R. Astron. Soc.* **358**(3), 716–725 (2005) <https://doi.org/10.1111/j.1365-2966.2005.08809.x> arXiv:astro-ph/0501142 [astro-ph]
- [13] Glebbeek, E., Pols, O.R., Hurley, J.R.: Evolution of stellar collision products in open clusters. I. Blue stragglers in N-body models of M 67. *Astron. Astrophys.* **488**(3), 1007–1015 (2008) <https://doi.org/10.1051/0004-6361:200809930> arXiv:0806.0863 [astro-ph]
- [14] Glebbeek, E., Gaburov, E., Portegies Zwart, S., Pols, O.R.: Structure and evolution of high-mass stellar mergers. *Mon. Not. R. Astron. Soc.* **434**(4), 3497–3510 (2013) <https://doi.org/10.1093/mnras/stt1268> arXiv:1307.2445 [astro-ph.SR]
- [15] Ryu, T., de Mink, S.E., Farmer, R., Pakmor, R., Perna, R., Springel, V.: Close encounters of star-black hole binaries with single stars. *Mon. Not. R. Astron. Soc.* **527**(2), 2734–2749 (2024) <https://doi.org/10.1093/mnras/stad3082> arXiv:2307.03097 [astro-ph.HE]
- [16] Weber, E.J., Davis, J. Leverett: The Angular Momentum of the Solar Wind. *Astrophys. J.* **148**, 217–227 (1967) <https://doi.org/10.1086/149138>
- [17] Leonard, P.J.T., Livio, M.: The Rotational Rates of Blue Stragglers Produced by Physical Stellar Collisions. *Astrophys. J. Lett.* **447**, 121 (1995) <https://doi.org/10.1086/309581>
- [18] Eggenberger, P., Maeder, A., Meynet, G.: Stellar evolution with rotation and magnetic fields. IV. The solar rotation profile. *Astron. Astrophys.* **440**(1), 9–12 (2005) <https://doi.org/10.1051/0004-6361:200500156> arXiv:astro-ph/0508455 [astro-ph]
- [19] Takahashi, K., Langer, N.: Modeling of magneto-rotational stellar evolution. I. Method and first applications. *Astron. Astrophys.* **646**, 19 (2021) <https://doi.org/10.1051/0004-6361/202039253> arXiv:2010.13909 [astro-ph.SR]
- [20] Cohen, J.G.: The velocity dispersion of the globular clusters in the Fornax dwarf

- galaxy. *Astrophys. J. Lett.* **270**, 41–42 (1983) <https://doi.org/10.1086/184066>
- [21] Springel, V.: E pur si muove: Galilean-invariant cosmological hydrodynamical simulations on a moving mesh. *Mon. Not. R. Astron. Soc.* **401**(2), 791–851 (2010) <https://doi.org/10.1111/j.1365-2966.2009.15715.x> arXiv:0901.4107 [astro-ph.CO]
- [22] Weinberger, R., Springel, V., Pakmor, R.: The AREPO Public Code Release. *Astrophys. J. Suppl.* **248**(2), 32 (2020) <https://doi.org/10.3847/1538-4365/ab908c> arXiv:1909.04667 [astro-ph.IM]
- [23] Pakmor, R., Springel, V., Bauer, A., Mocz, P., Munoz, D.J., Ohlmann, S.T., Schaal, K., Zhu, C.: Improving the convergence properties of the moving-mesh code AREPO. *Mon. Not. R. Astron. Soc.* **455**(1), 1134–1143 (2016) <https://doi.org/10.1093/mnras/stv2380> arXiv:1503.00562 [astro-ph.GA]
- [24] VandenBerg, D.A., Brogaard, K., Leaman, R., Casagrande, L.: The Ages of 55 Globular Clusters as Determined Using an Improved $\delta V_{TO}^{\text{HB}}$ Method Along with Color-Magnitude Diagram Constraints, and Their Implications for Broader Issues. *ApJ* **775**(2), 134 (2013) <https://doi.org/10.1088/0004-637X/775/2/134>
- [25] Hale, G.E.: Preliminary Results of an Attempt to Detect the General Magnetic Field of the Sun. *Astrophys. J.* **38**, 27 (1913) <https://doi.org/10.1086/142013>
- [26] Babcock, H.W., Babcock, H.D.: The Sun’s Magnetic Field, 1952-1954. *Astrophys. J.* **121**, 349 (1955) <https://doi.org/10.1086/145994>
- [27] Alfvén, H.: The Sun’s General Magnetic Field. *Tellus* **8**(1), 2–12 (1956) <https://doi.org/10.3402/tellusa.v8i1.8946>
- [28] Reiners, A., Shulyak, D., Käpylä, P.J., Ribas, I., Nagel, E., Zechmeister, M., Caballero, J.A., Shan, Y., Fuhrmeister, B., Quirrenbach, A., Amado, P.J., Montes, D., Jeffers, S.V., Azzaro, M., Béjar, V.J.S., Chaturvedi, P., Henning, T., Kürster, M., Pallé, E.: Magnetism, rotation, and nonthermal emission in cool stars. Average magnetic field measurements in 292 M dwarfs. *Astron. Astrophys.* **662**, 41 (2022) <https://doi.org/10.1051/0004-6361/202243251> arXiv:2204.00342 [astro-ph.SR]
- [29] Pakmor, R., Bieri, R., van de Voort, F., Werhahn, M., Fattahi, A., Guillet, T., Pfrommer, C., Springel, V., Talbot, R.Y.: Magnetic field amplification in cosmological zoom simulations from dwarf galaxies to galaxy groups. *Mon. Not. R. Astron. Soc.* **528**(2), 2308–2325 (2024) <https://doi.org/10.1093/mnras/stae112> arXiv:2309.13104 [astro-ph.GA]
- [30] Schneider, F.R.N., Ohlmann, S.T., Podsiadlowski, P., Röpke, F.K., Balbus, S.A., Pakmor, R., Springel, V.: Stellar mergers as the origin of magnetic massive stars.

- Nature **574**(7777), 211–214 (2019) <https://doi.org/10.1038/s41586-019-1621-5> [arXiv:1910.14058](https://arxiv.org/abs/1910.14058) [astro-ph.SR]
- [31] Kiuchi, K., Reboul-Salze, A., Shibata, M., Sekiguchi, Y.: A large-scale magnetic field produced by a solar-like dynamo in binary neutron star mergers. *Nature Astronomy* **8**, 298–307 (2024) <https://doi.org/10.1038/s41550-024-02194-y> [arXiv:2306.15721](https://arxiv.org/abs/2306.15721) [astro-ph.HE]
- [32] Cattaneo, F.: On the Origin of Magnetic Fields in the Quiet Photosphere. *Astrophys. J. Lett.* **515**(1), 39–42 (1999) <https://doi.org/10.1086/311962>
- [33] Federrath, C.: Magnetic field amplification in turbulent astrophysical plasmas. *Journal of Plasma Physics* **82**(6), 535820601 (2016) <https://doi.org/10.1017/S0022377816001069> [arXiv:1610.08132](https://arxiv.org/abs/1610.08132) [physics.plasm-ph]
- [34] Kriel, N., Beattie, J.R., Federrath, C., Krumholz, M.R., Hew, J.K.J.: Fundamental MHD scales – II: the kinematic phase of the supersonic small-scale dynamo. *arXiv e-prints*, 2310–17036 (2023) <https://doi.org/10.48550/arXiv.2310.17036> [arXiv:2310.17036](https://arxiv.org/abs/2310.17036) [astro-ph.GA]
- [35] Beattie, J.R., Federrath, C., Kriel, N., Mocz, P., Seta, A.: Growth or Decay - I: universality of the turbulent dynamo saturation. *Mon. Not. R. Astron. Soc.* **524**(3), 3201–3214 (2023) <https://doi.org/10.1093/mnras/stad1863> [arXiv:2209.10749](https://arxiv.org/abs/2209.10749) [astro-ph.GA]
- [36] Safier, P.N.: A Critique of Current Magnetic-Accretion Models for Classical T Tauri Stars. *Astrophys. J.* **494**(1), 336–341 (1998) <https://doi.org/10.1086/305212> [arXiv:astro-ph/9709158](https://arxiv.org/abs/astro-ph/9709158) [astro-ph]
- [37] Matt, S., Pudritz, R.E.: Does Disk Locking Solve the Stellar Angular Momentum Problem? *Astrophys. J. Lett.* **607**(1), 43–46 (2004) <https://doi.org/10.1086/421351> [arXiv:astro-ph/0403635](https://arxiv.org/abs/astro-ph/0403635) [astro-ph]
- [38] Benz, W., Hills, J.G.: Three-dimensional Hydrodynamical Simulations of Stellar Collisions. I. Equal-Mass Main-Sequence Stars. *Astrophys. J.* **323**, 614 (1987) <https://doi.org/10.1086/165857>
- [39] Justham, S., Rappaport, S., Podsiadlowski, P.: Magnetic braking of Ap/Bp stars: application to compact black-hole X-ray binaries. *Mon. Not. R. Astron. Soc.* **366**(4), 1415–1423 (2006) <https://doi.org/10.1111/j.1365-2966.2005.09907.x> [arXiv:astro-ph/0511760](https://arxiv.org/abs/astro-ph/0511760) [astro-ph]
- [40] Matt, S.P., MacGregor, K.B., Pinsonneault, M.H., Greene, T.P.: Magnetic Braking Formulation for Sun-like Stars: Dependence on Dipole Field Strength and Rotation Rate. *Astrophys. J. Lett.* **754**(2), 26 (2012) <https://doi.org/10.1088/2041-8205/754/2/L26> [arXiv:1206.2354](https://arxiv.org/abs/1206.2354) [astro-ph.SR]

- [41] Ferraro, F.R., Mucciarelli, A., Lanzoni, B., Pallanca, C., Cadelano, M., Billi, A., Sills, A., Vesperini, E., Dalessandro, E., Beccari, G., Monaco, L., Mateo, M.: Fast rotating blue stragglers prefer loose clusters. *Nature Communications* **14**, 2584 (2023) <https://doi.org/10.1038/s41467-023-38153-w> arXiv:2305.08478 [astro-ph.SR]
- [42] Rincon, F.: Dynamo theories. *Journal of Plasma Physics* **85**(4), 205850401 (2019) <https://doi.org/10.1017/S0022377819000539> arXiv:1903.07829 [physics.plasm-ph]
- [43] Schekochihin, A.A., Cowley, S.C., Taylor, S.F., Maron, J.L., McWilliams, J.C.: Simulations of the Small-Scale Turbulent Dynamo. *Astrophys. J.* **612**(1), 276–307 (2004) <https://doi.org/10.1086/422547> arXiv:astro-ph/0312046 [astro-ph]
- [44] Iskakov, A.B., Schekochihin, A.A., Cowley, S.C., McWilliams, J.C., Proctor, M.R.E.: Numerical Demonstration of Fluctuation Dynamo at Low Magnetic Prandtl Numbers. *Phys. Rev. Lett.* **98**(20), 208501 (2007) <https://doi.org/10.1103/PhysRevLett.98.208501> arXiv:astro-ph/0702291 [astro-ph]
- [45] Warnecke, J., Korpi-Lagg, M.J., Gent, F.A., Rheinhardt, M.: Numerical evidence for a small-scale dynamo approaching solar magnetic Prandtl numbers. *Nature Astronomy* **7**, 662–668 (2023) <https://doi.org/10.1038/s41550-023-01975-1> arXiv:2306.03991 [astro-ph.SR]
- [46] Spitzer, L.: *Physics of Fully Ionized Gases*, (1962)
- [47] Paxton, B., Bildsten, L., Dotter, A., Herwig, F., Lesaffre, P., Timmes, F.: Modules for Experiments in Stellar Astrophysics (MESA). *Astrophys. J. Suppl.* **192**, 3 (2011) <https://doi.org/10.1088/0067-0049/192/1/3> arXiv:1009.1622 [astro-ph.SR]
- [48] Paxton, B., Cantiello, M., Arras, P., Bildsten, L., Brown, E.F., Dotter, A., Mankovich, C., Montgomery, M.H., Stello, D., Timmes, F.X., Townsend, R.: Modules for Experiments in Stellar Astrophysics (MESA): Planets, Oscillations, Rotation, and Massive Stars. *Astrophys. J. Suppl.* **208**, 4 (2013) <https://doi.org/10.1088/0067-0049/208/1/4> arXiv:1301.0319 [astro-ph.SR]
- [49] Paxton, B., Marchant, P., Schwab, J., Bauer, E.B., Bildsten, L., Cantiello, M., Dessart, L., Farmer, R., Hu, H., Langer, N., Townsend, R.H.D., Townsley, D.M., Timmes, F.X.: Modules for Experiments in Stellar Astrophysics (MESA): Binaries, Pulsations, and Explosions. *Astrophys. J. Suppl.* **220**, 15 (2015) <https://doi.org/10.1088/0067-0049/220/1/15> arXiv:1506.03146 [astro-ph.SR]
- [50] Paxton, B., Smolec, R., Schwab, J., Gaultschi, A., Bildsten, L., Cantiello, M., Dotter, A., Farmer, R., Goldberg, J.A., Jermyn, A.S., Kanbur, S.M., Marchant, P., Thoul, A., Townsend, R.H.D., Wolf, W.M., Zhang, M., Timmes, F.X.: Modules for Experiments in Stellar Astrophysics (MESA): Pulsating Variable Stars,

- Rotation, Convective Boundaries, and Energy Conservation. *Astrophys. J. Suppl.* **243**(1), 10 (2019) <https://doi.org/10.3847/1538-4365/ab2241> arXiv:1903.01426 [astro-ph.SR]
- [51] Jermyn, A.S., Bauer, E.B., Schwab, J., Farmer, R., Ball, W.H., Bellinger, E.P., Dotter, A., Joyce, M., Marchant, P., Mombarg, J.S.G., Wolf, W.M., Sunny Wong, T.L., Cinquegrana, G.C., Farrell, E., Smolec, R., Thoul, A., Cantiello, M., Herwig, F., Toloza, O., Bildsten, L., Townsend, R.H.D., Timmes, F.X.: Modules for Experiments in Stellar Astrophysics (MESA): Time-dependent Convection, Energy Conservation, Automatic Differentiation, and Infrastructure. *Astrophys. J. Suppl.* **265**(1), 15 (2023) <https://doi.org/10.3847/1538-4365/aca8d> arXiv:2208.03651 [astro-ph.SR]
- [52] Choi, J., Dotter, A., Conroy, C., Cantiello, M., Paxton, B., Johnson, B.D.: Mesa Isochrones and Stellar Tracks (MIST). I. Solar-scaled Models. *Astrophys. J.* **823**(2), 102 (2016) <https://doi.org/10.3847/0004-637X/823/2/102> arXiv:1604.08592 [astro-ph.SR]
- [53] Ledoux, W.P.: Stellar Models with Convection and with Discontinuity of the Mean Molecular. *ApJ* **105**, 305 (1947) <https://doi.org/10.1086/144905>
- [54] Vogelsberger, M., Genel, S., Springel, V., Torrey, P., Sijacki, D., Xu, D., Snyder, G., Nelson, D., Hernquist, L.: Introducing the Illustris Project: simulating the coevolution of dark and visible matter in the Universe. *Mon. Not. R. Astron. Soc.* **444**(2), 1518–1547 (2014) <https://doi.org/10.1093/mnras/stu1536> arXiv:1405.2921 [astro-ph.CO]
- [55] Springel, V., Pakmor, R., Pillepich, A., Weinberger, R., Nelson, D., Hernquist, L., Vogelsberger, M., Genel, S., Torrey, P., Marinacci, F., Naiman, J.: First results from the IllustrisTNG simulations: matter and galaxy clustering. *Mon. Not. R. Astron. Soc.* **475**(1), 676–698 (2018) <https://doi.org/10.1093/mnras/stx3304> arXiv:1707.03397 [astro-ph.GA]
- [56] Vynatheya, P., Ryu, T., Pakmor, R., de Mink, S.E., Perets, H.B.: Simulating the tidal disruption of stars by stellar-mass black holes using moving-mesh hydrodynamics. *arXiv e-prints*, 2310–14852 (2023) <https://doi.org/10.48550/arXiv.2310.14852> arXiv:2310.14852 [astro-ph.HE]
- [57] Xin, C., Haiman, Z., Perna, R., Wang, Y., Ryu, T.: Tidal Peeling Events: low-eccentricity tidal disruption of a star by a stellar-mass black hole. *arXiv e-prints*, 2303–12846 (2023) <https://doi.org/10.48550/arXiv.2303.12846> arXiv:2303.12846 [astro-ph.HE]
- [58] Ryu, T., McKernan, B., Ford, K.E.S., Cantiello, M., Graham, M., Stern, D., Leigh, N.W.C.: In-plane tidal disruption of stars in discs of active galactic nuclei. *Mon. Not. R. Astron. Soc.* **527**(3), 8103–8117 (2024) <https://doi.org/10.1093/mnras/stad3487> arXiv:2310.00610 [astro-ph.HE]

- [59] Ohlmann, S.T., Röpke, F.K., Pakmor, R., Springel, V., Müller, E.: Magnetic field amplification during the common envelope phase. *Mon. Not. R. Astron. Soc.* **462**(1), 121–125 (2016) <https://doi.org/10.1093/mnrasl/slw144> arXiv:1607.05996 [astro-ph.SR]
- [60] Pakmor, R., Kromer, M., Taubenberger, S., Sim, S.A., Röpke, F.K., Hillebrandt, W.: Normal Type Ia Supernovae from Violent Mergers of White Dwarf Binaries. *Astrophys. J. Lett.* **747**(1), 10 (2012) <https://doi.org/10.1088/2041-8205/747/1/L10> arXiv:1201.5123 [astro-ph.HE]
- [61] Pakmor, R., Pelisoli, I., Justham, S., Rajamuthukumar, A.S., Röpke, F.K., Schneider, F.R.N., de Mink, S.E., Ohlmann, S.T., Podsiadlowski, P., Moran Fraile, J., Vetter, M., Androssy, R.: Large-scale ordered magnetic fields generated in mergers of helium white dwarfs. arXiv e-prints, 2407–02566 (2024) <https://doi.org/10.48550/arXiv.2407.02566> arXiv:2407.02566 [astro-ph.SR]
- [62] Ryu, T., Amaro Seoane, P., Taylor, A.M., Ohlmann, S.T.: Collisions of red giants in galactic nuclei. *Mon. Not. R. Astron. Soc.* **528**(4), 6193–6209 (2024) <https://doi.org/10.1093/mnras/stae396> arXiv:2307.07338 [astro-ph.HE]
- [63] Rogers, F.J., Nayfonov, A.: Updated and Expanded OPAL Equation-of-State Tables: Implications for Helioseismology. *Astrophys. J.* **576**(2), 1064–1074 (2002) <https://doi.org/10.1086/341894>
- [64] Powell, K.G., Roe, P.L., Linde, T.J., Gombosi, T.I., De Zeeuw, D.L.: A Solution-Adaptive Upwind Scheme for Ideal Magnetohydrodynamics. *Journal of Computational Physics* **154**(2), 284–309 (1999) <https://doi.org/10.1006/jcph.1999.6299>
- [65] Pakmor, R., Bauer, A., Springel, V.: Magnetohydrodynamics on an unstructured moving grid. *Mon. Not. R. Astron. Soc.* **418**(2), 1392–1401 (2011) <https://doi.org/10.1111/j.1365-2966.2011.19591.x> arXiv:1108.1792 [astro-ph.IM]
- [66] Pakmor, R., Springel, V.: Simulations of magnetic fields in isolated disc galaxies. *Mon. Not. R. Astron. Soc.* **432**(1), 176–193 (2013) <https://doi.org/10.1093/mnras/stt428> arXiv:1212.1452 [astro-ph.CO]
- [67] Ohlmann, S.T., Röpke, F.K., Pakmor, R., Springel, V.: Constructing stable 3D hydrodynamical models of giant stars. *Astron. Astrophys.* **599**, 5 (2017) <https://doi.org/10.1051/0004-6361/201629692> arXiv:1612.00008 [astro-ph.SR]
- [68] Lombardi, J. James C., Rasio, F.A., Shapiro, S.L.: Collisions of Main-Sequence Stars and the Formation of Blue Stragglers in Globular Clusters. *Astrophys. J.* **468**, 797 (1996) <https://doi.org/10.1086/177736> arXiv:astro-ph/9511074 [astro-ph]

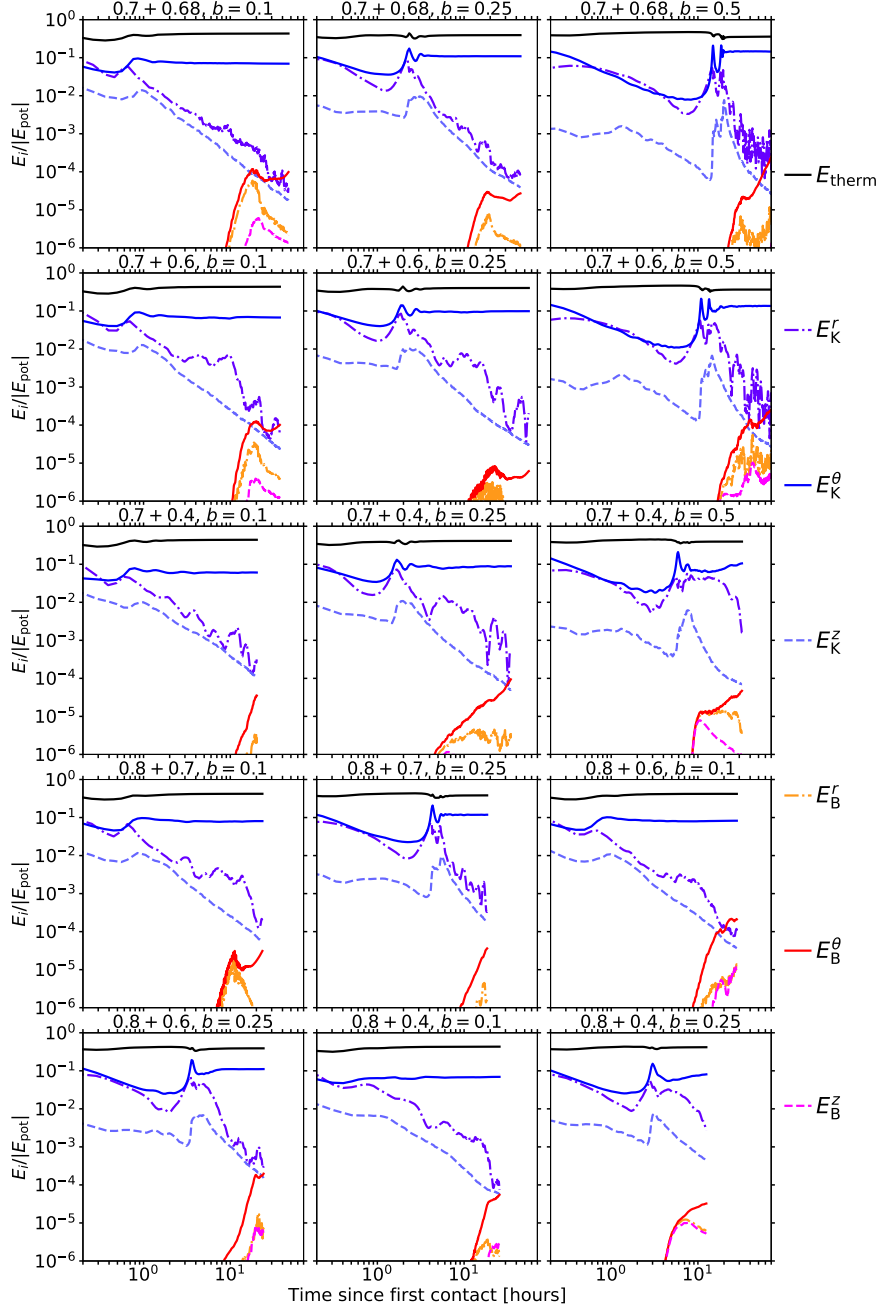


Fig. C4 Ratios of the thermal (E_{therm} , black solid), kinetic (E_K , blue-family lines), and magnetic (E_B , red-family lines) energy to the absolute potential energy $|E_{\text{pot}}|$, as a function of time since the first contact. There is a clear energy hierarchy such that $E_{\text{pot}} > E_{\text{therm}} > E_K \gg E_B$. The sum of the thermal (E_{therm}) and kinetic energy (E_K) is $\simeq 0.5|E_{\text{pot}}|$, while $E_{\text{therm}}/E_K \simeq 3-4$. In addition, each component of E_K and E_B reveals a similar hierarchical structure, independent of the collision parameters: $E_K^\theta \gg E_K^r \simeq E_K^z (\lesssim 1\%)$ and $E_B^\theta \gg E_B^r \simeq E_B^z (\lesssim 10\%)$.

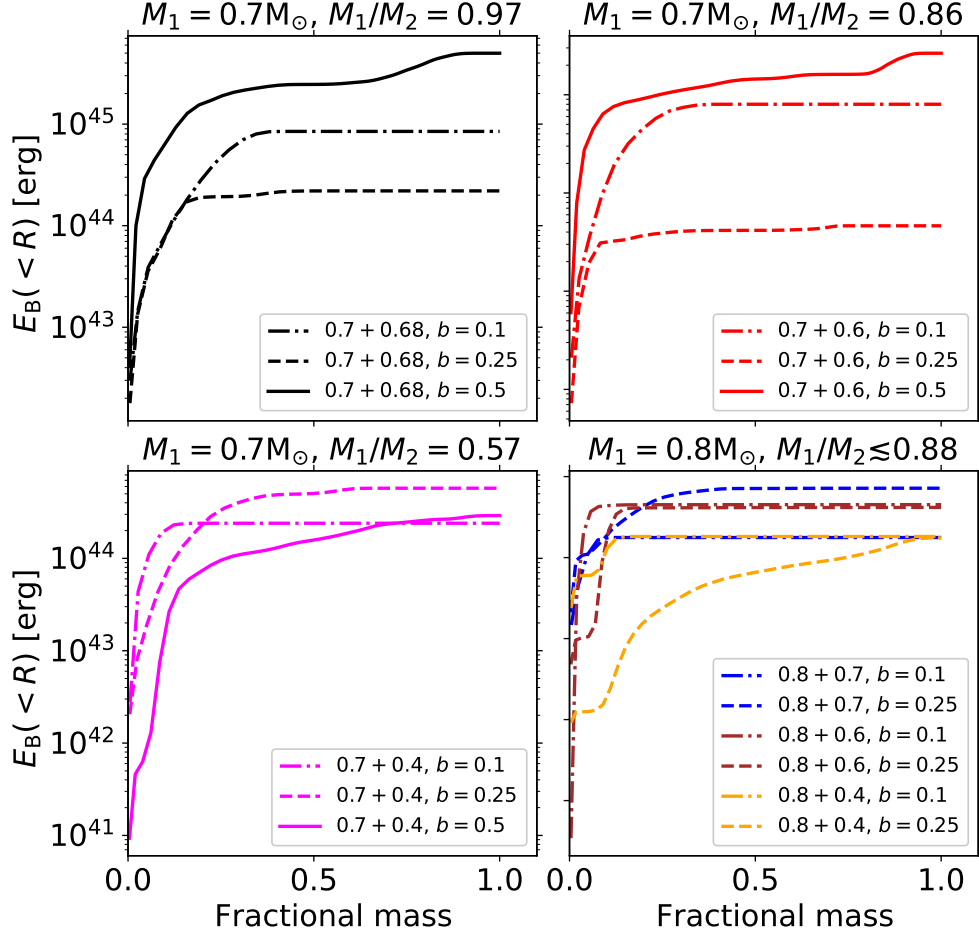


Fig. C5 Accumulative magnetic field energy $E_B(<R)$, as a function of the fractional enclosed mass, for all the models. $M_1 = 0.7 M_\odot, q = M_2/M_1 = 0.97$ (top-left), $M_1 = 0.7 M_\odot, q = 0.86$ (top-right), $M_1 = 0.7 M_\odot, q = 0.57$ (bottom-left), and $M_1 = 0.8 M_\odot, q \lesssim 0.88$ (bottom-right). Most of E_B is contained within inner 20-30% of the mass for $b \leq 0.25$ and inner 90% for $b = 0.5$.

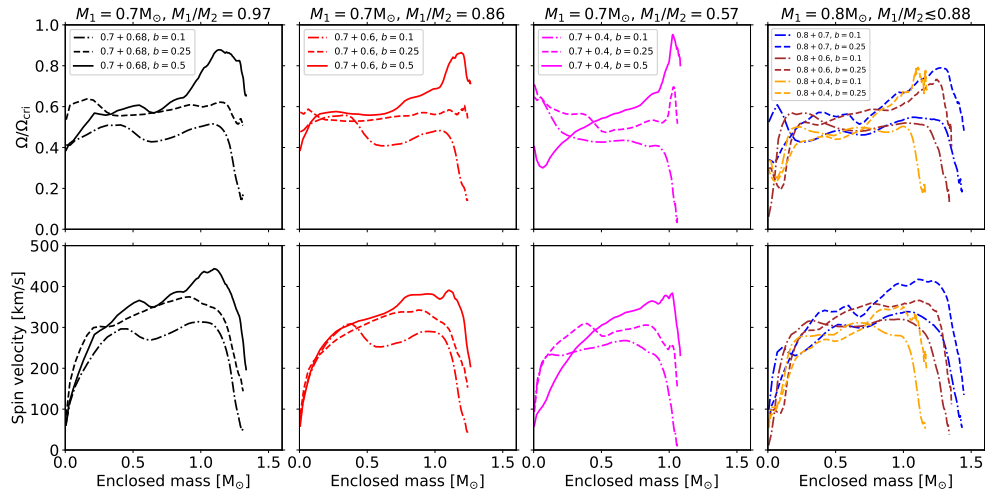


Fig. D6 Spin frequency with respect to the critical frequency (top) and mid-plane spin velocity (bottom) in all our models, as a function of enclosed mass. The models are divided into four groups depending on the primary mass and mass ratios: $M_1 = 0.7 M_{\odot}, q = M_2/M_1 = 0.97$ (left-most), $M_1 = 0.7 M_{\odot}, q = 0.86$ (left-middle), $M_1 = 0.7 M_{\odot}, q = 0.57$ (right-middle), and $M_1 = 0.8 M_{\odot}, q \lesssim 0.88$ (right-most).

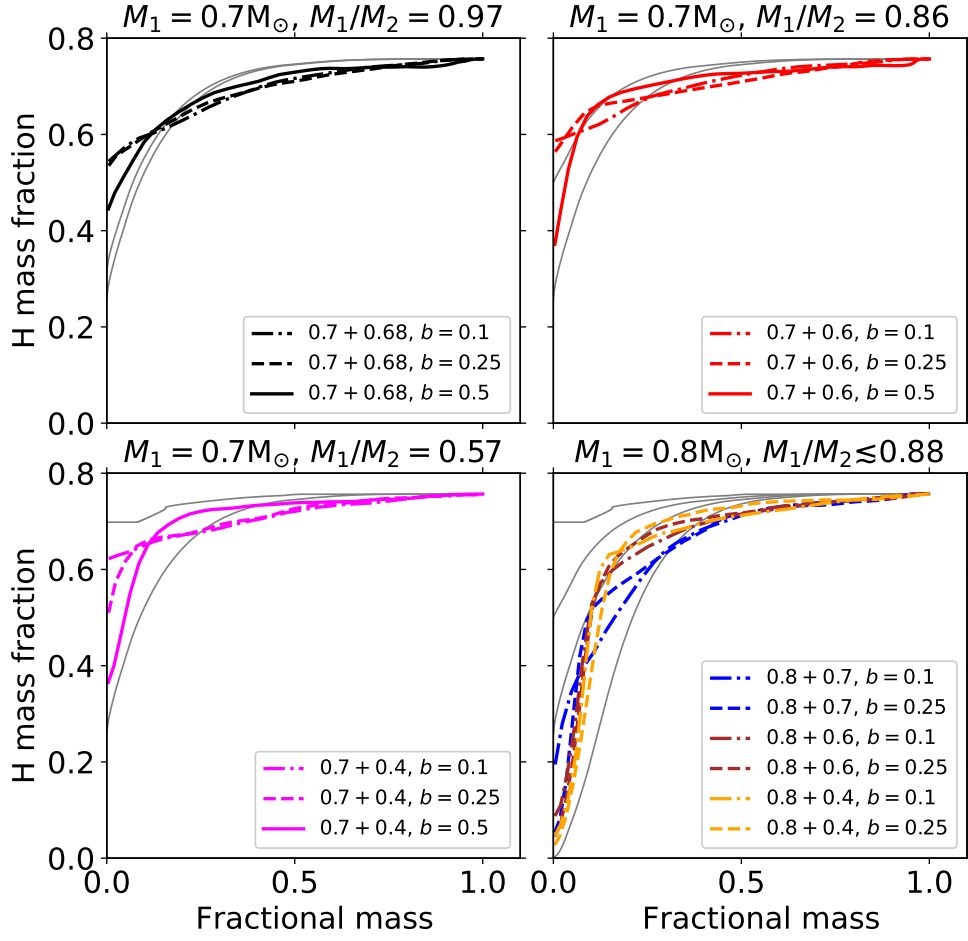


Fig. D7 Mass-weighted average of the hydrogen mass fraction within the collision products, as a function of enclosed mass. The models are divided into four groups depending on the primary mass and mass ratio: $M_1 = 0.7M_\odot, q = M_2/M_1 = 0.97$ (top-left), $M_1 = 0.7M_\odot, q = 0.86$ (top-right), $M_1 = 0.7M_\odot, q = 0.57$ (bottom-left), and $M_1 = 0.8M_\odot, q \lesssim 0.88$ (bottom-right). The grey lines in each top panel indicate the profiles of the initial stars: less massive stars have higher core hydrogen mass fraction at the same age.

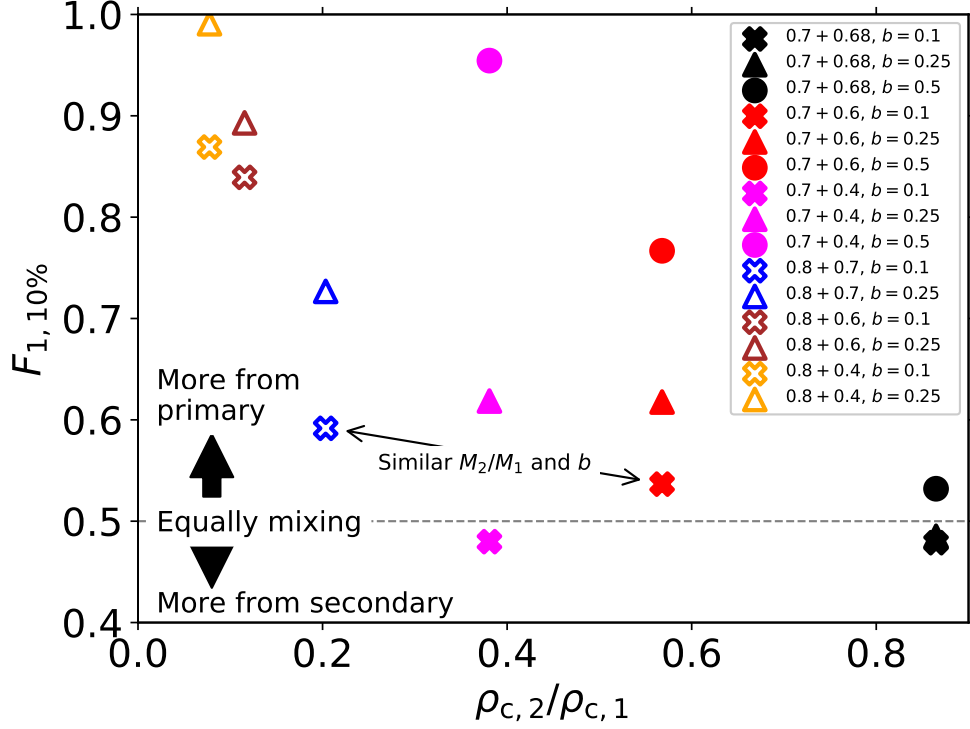


Fig. D8 Fraction of mass in the central part of collision products (inner 10% in mass) that originally belonged to the primary star $F_{1,10\%}$, as a function of the core density ratio of the original two stars. $F_{1,10\%} = 0.5$ (horizontal grey line) indicates that two stars are equally mixed, while $F_{1,10\%} > 0.5$ indicates that the chemical abundances in more than 50% of the central part originated from the primary. The collisions with the same mass ratio (impact parameter b) share the same color (shape). We further differentiate collisions with the primary mass $M_1 = 0.7 M_\odot$ (solid markers) from those with $M_1 = 0.8 M_\odot$ (hollow markers). The general trend is that mixing becomes more efficient ($F_{1,10\%} \rightarrow 0.5$) if collisions occur between stars with similar masses and smaller b . In addition, collisions of a primary star which is easily destroyed (lower central density or higher core H mass fraction) lead to efficient mixing, indicated by generally smaller $F_{1,10\%}$ for $M_1 = 0.7 M_\odot$ than that for $M_1 = 0.8 M_\odot$.

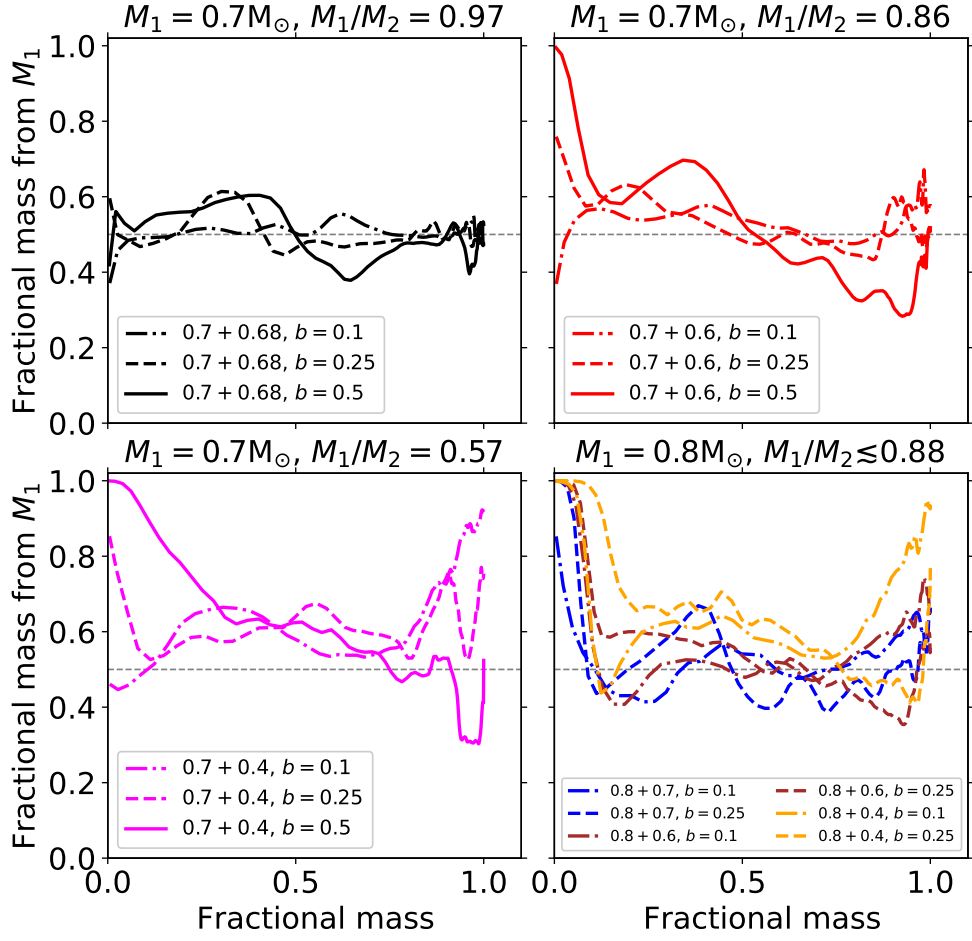


Fig. D9 Fraction of mass that originally belonged to the primary, as a function of the enclosed mass. The models are divided into four groups depending on the primary mass and mass ratios: $M_1 = 0.7M_\odot, q = M_2/M_1 = 0.97$ (top-left), $M_1 = 0.7M_\odot, q = 0.86$ (top-right), $M_1 = 0.7M_\odot, q = 0.57$ (bottom-left), and $M_1 = 0.8M_\odot, q \lesssim 0.88$ (bottom-right). The factor of 0.5, indicated by the grey horizontal line in each top panel, indicates that the chemical abundances at the mass bin equally originate from both parent two stars.

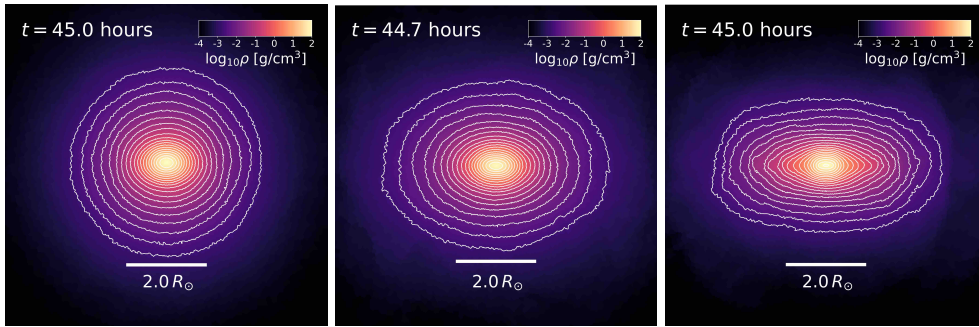


Fig. E10 Density distribution of the products in collisions between a $0.7 M_{\odot}$ star and $0.68 M_{\odot}$ star with $b = 0.1$ (left), 0.25 (middle), and 0.5 (right) along an $x - z$ slice passing through the center of mass, overlaid with equidensity lines (white contours). The density is measured at $t \simeq 45$ hours since the first contact. As b increases, the overall shape of the product becomes more oblate because of larger angular momentum. Markedly, for $b = 0.5$, a noticeably flattened structure along the mid-plane appears between the central part of the product and the outermost envelope, potentially indicative of disk formation.